

# Lawrence Berkeley National Laboratory

## LBL Publications

### Title

Impact of Distinct Origin Locations on the Life Cycles of Landfalling Atmospheric Rivers Over the U.S. West Coast

### Permalink

<https://escholarship.org/uc/item/31b6z0pm>

### Journal

Journal of Geophysical Research: Atmospheres, 124(22)

### ISSN

2169-897X

### Authors

Zhou, Yang  
Kim, Hyemi

### Publication Date

2019-11-27

### DOI

10.1029/2019jd031218

Peer reviewed

1           **Impact of Distinct Origin Locations on the Life Cycles of Landfalling**  
2                           **Atmospheric Rivers over the U.S. West Coast**

3  
4   Yang Zhou<sup>1</sup> and Hyemi Kim<sup>2</sup>

5   <sup>1</sup>Lawrence Berkeley National Laboratory, Berkeley, CA

6   <sup>2</sup>School of Marine and Atmospheric Sciences, Stony Brook University, Stony Brook, NY

7  
8           Corresponding author: Hyemi Kim ([hyemi.kim@stonybrook.edu](mailto:hyemi.kim@stonybrook.edu))

9  
10  
11  
12  
13  
14  
15   **Key Points:**

- 16           • U.S. West Coast landfalling AR events originating from the Northwest Pacific are  
17                   stronger with longer lifetime than those from the Northeast
- 18           • A persistent tripole geopotential height anomaly pattern modulates the life cycles of  
19                   landfalling AR events from distinct origin locations
- 20           • Landfalling AR events originating from the Northwest (Northeast) Pacific induce  
21                   precipitation over the northern (southern) U.S. West Coast

22  
23  
24  
25  
26  
27  
28  
29  
30  
31  
32  
33  
34  
35  
36  
37  
38  
39  
40  
41

**Abstract**

An atmospheric river (AR) event represents strong poleward moisture transport and is defined as a series of spatiotemporally connected instantaneous AR objects. Utilizing an AR tracking algorithm with a depth-first search (a widely-used algorithm in computer science), we examine the life-cycle characteristics of AR events that make landfall over the U.S. West Coast by their distinct origin locations. Landfalling AR events from the Northwest Pacific (120°E-170°W, WLAR events) temporally last longer (5.3 days vs. 3.6 days on average) and have stronger intensity of integrated vapor transport ( $508 \text{ kg m}^{-1} \text{ s}^{-1}$  vs.  $388 \text{ kg m}^{-1} \text{ s}^{-1}$  on average) than those originating from the Northeast Pacific (125°W-170°W, ELAR events). A persistent tripole geopotential height anomaly pattern over the North Pacific modulates the origin locations and propagation of landfalling AR events. WLAR events are associated with anomalous highs over northeastern Asia and the Northeast Pacific and an anomalous low over the central North Pacific. This pattern provides favorable conditions for WLAR events to start, propagate northeastward, and make landfall in the northwestern West Coast. WLAR events contribute approximately 25% of the total winter precipitation over Washington and British Columbia. ELAR events are associated with the nearly opposite tripole pattern to the WLAR events. The anomalous low over the Northeast Pacific helps ELAR events to start, propagate northeastward, and make landfall in the southwestern West Coast. Precipitation induced by ELAR events contributes up to 30% of total winter precipitation over California.

42  
43  
44  
45  
46  
47  
48  
49  
50  
51

### **Plain Language Summary**

Atmospheric rivers (ARs) are strong poleward water vapor transport events in the lower troposphere. AR events are important to water resources over the U.S. West Coast. We compared the characteristics, circulation patterns, and precipitation of landfalling AR events over the U.S. West Coast based on their origin locations. In general, landfalling AR events originating from the Northwest Pacific (120°E-170°W) last longer and have stronger intensities than those from the Northeast Pacific (125°W-170°W). The life cycles (origin, propagation, and termination) of landfalling AR events and AR-related precipitation are strongly modulated by large-scale tripole geopotential height anomaly pattern over the North Pacific basin.

52 **1 Introduction**

53 Atmospheric rivers (ARs) are filamentary plumes of intensive poleward water vapor  
54 transport in the atmosphere that play an essential role in the global hydrological cycle (Zhu &  
55 Newell, 1994, 1998). ARs are important to coastal water resources, especially over the U.S. West  
56 Coast, where they account for approximately 30-50% of precipitation and snow water equivalent  
57 over the region (Dettinger et al., 2011; Guan et al., 2010, 2013; J. Kim et al., 2013; Lavers &  
58 Villarini, 2015). About 30-70% of West Coast droughts were ended by AR-related storms  
59 (Dettinger, 2013). Strong ARs are associated with heavy precipitation and disastrous events such  
60 as floods and extreme winds (Dettinger et al., 2011; Neiman et al., 2013; Ralph et al., 2013;  
61 Ralph & Dettinger, 2012; Ralph et al., 2006; Smith et al., 2010; Waliser & Guan, 2017). The  
62 number of landfalling ARs and their associated precipitation over the U.S. West Coast are  
63 projected to increase with global warming (Dettinger, 2011; Espinoza et al., 2018; Gershunov et  
64 al., 2019; Hagos et al., 2016; Lavers et al., 2013; Payne & Magnusdottir, 2015; Warner et al.,  
65 2015), which may cause significant economic loss (Dominguez et al., 2018). Therefore, a better  
66 understanding of landfalling ARs over the U.S. West Coast and their regional impacts is crucial  
67 for accurate predictions and projections of AR-related weather hazards, which could help  
68 policymakers and emergency managers to prepare mitigating actions in advance. Given the  
69 significant socio-economic impacts of ARs, the characteristics and variability of ARs and the  
70 associated physical mechanisms (e.g. Guan & Waliser, 2015; H. Kim et al., 2017; Mundhenk et  
71 al., 2016a; Mundhenk et al., 2016b; Payne & Magnusdottir, 2014; Ryoo et al., 2013; Ryoo et al.,  
72 2015 and review by Gimeno et al., 2014 and Shields et al., 2018) as well as the prediction of  
73 ARs (e.g. DeFlorio et al., 2018a; DeFlorio et al., 2018b; Mundhenk et al., 2018; Nardi et al.,  
74 2018; Wick et al., 2013; Zhou & Kim, 2017) have been widely investigated.

75 Most of the previous studies have focused on the characteristics of landfalling AR events  
76 during a relatively short period (about 24-72 hours) during landfall rather than analyzing their  
77 entire life cycles from origin to termination (e.g. Neiman et al., 2013; Rutz et al., 2014; Waliser  
78 & Guan, 2017). A handful of studies focusing on the entire life cycles of landfalling ARs have  
79 been limited to case studies or specific features of AR life cycles, such as intensity or spatial  
80 distributions of origin and termination. For example, Ralph et al. (2011) used observational data  
81 to track the evolution of a single landfalling AR event over the U.S. West Coast during March  
82 2005 and linked its life cycle with multi-scale dynamical processes such as mesoscale frontal  
83 waves and the Madden-Julian Oscillation (MJO). Since this study focused on a single case, it  
84 may not represent the general characteristics of the life cycles of landfalling AR events. By  
85 focusing on the intensities of landfalling ARs only, Payne and Magnusdottir (2014) showed that  
86 stronger landfalling AR events tend to originate from the western Pacific, while the weaker  
87 events originate from the eastern Pacific. Sellars et al. (2017) focused on the global distributions  
88 of origins and terminations of AR events and the association with climate variability, while other  
89 life-cycle characteristics such as lifetime and intensity of ARs were not examined.

90 In Zhou et al. (2018), an automated object tracking algorithm was developed that can  
91 identify the life-cycle characteristics of ARs such as the locations of origin and termination,  
92 lifetime, intensity, and the propagation track. While the general characteristics of AR life cycles  
93 over the entire North Pacific have been discussed in Zhou et al. (2018), a detailed analysis that  
94 specifically targets landfalling AR events over the U.S. West Coast has yet to be conducted.  
95 Depending on their origin locations (Northwest (120°E-170°W) vs. Northeast Pacific (125°W-  
96 170°W)), landfalling AR events may have distinct characteristics in intensity, propagation  
97 pathway, and precipitation location. In this study, the impact of distinct origin locations on the

98 life-cycle characteristics of landfalling AR events over the U.S. West Coast will be examined in  
 99 detail by adopting the AR tracking algorithm from Zhou et al. (2018). Data selection and the  
 100 updated tracking algorithm are introduced in section 2. Characteristics of landfalling AR events  
 101 from different origin locations are compared in section 3. In section 4, we discuss the evolution  
 102 of landfalling AR events originating from distinct locations and the corresponding large-scale  
 103 patterns. Spatiotemporal evolution of AR-induced precipitation is examined in section 5.  
 104 Summary and discussion are provided in section 6.

105

## 106 **2 Data and Tracking Algorithm**

### 107 **2.1 Data**

108 To detect ARs, we use the vertically-integrated water vapor transport (IVT), which is  
 109 calculated as:

$$110 \quad \text{IVT} = -\frac{1}{g} \int_{1000 \text{ hPa}}^{300 \text{ hPa}} q \vec{V} dp, \quad (1)$$

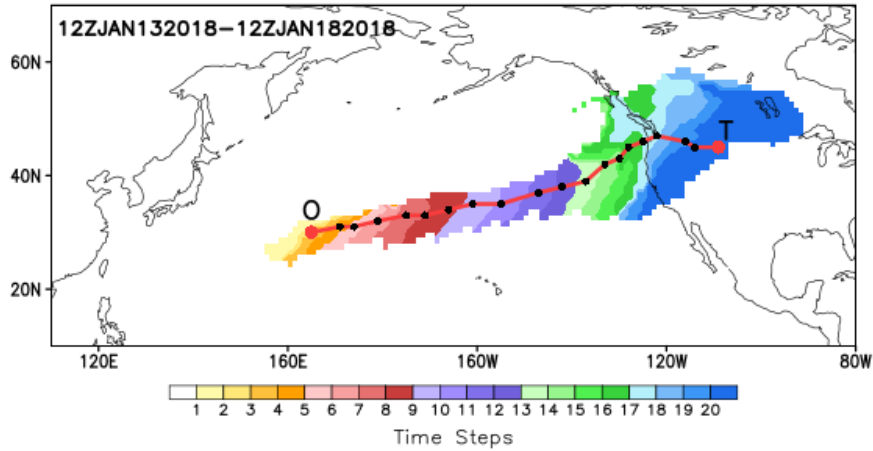
111 where  $g$  is gravitational acceleration ( $\text{m s}^{-2}$ ),  $p$  is pressure (hPa),  $q$  is specific humidity ( $\text{kg kg}^{-1}$ ),  
 112 and  $\vec{V}$  is the horizontal wind vector ( $\text{m s}^{-1}$ ). To calculate the IVT, 20 vertical levels (1000-300  
 113 hPa) of 6-hourly horizontal winds and specific humidity data from the European Centre for  
 114 Medium-Range Weather Forecasts Interim Reanalysis (ERA-Interim, (Dee et al., 2011)) are used with  
 115  $1.0^\circ$  horizontal grid spacing. To evaluate the evolution of landfalling AR events and circulation  
 116 patterns, daily (00Z) anomalous (minus daily climatology) horizontal winds, specific humidity,  
 117 and 500 hPa geopotential height from ERA-Interim are used. To examine the coastal  
 118 precipitation responses, CPC unified gauge-based analysis of  $0.5^\circ$  daily-mean anomalous  
 119 precipitation over land (Xie et al., 2007) is analyzed. We focus on 39 cool seasons (1979-2018)

120 from November to March, which is a relatively active season of landfalling ARs (Mundhenk et  
121 al., 2016a).

## 122 2.2 Tracking Algorithm: Depth-First Search

123 One of the approaches to detecting ARs is the “condition” parameter detection (Shields et  
124 al., 2018), which involves applying a set of conditions on the IVT field at every time step to  
125 identify an AR object. The AR object is defined as an enclosed two-dimensional (longitude and  
126 latitude) instantaneous area that meets the given AR-related conditions. In this study, we apply  
127 the AR detection method developed by Guan and Waliser (2015), who combined multiple  
128 conditions including IVT magnitude, IVT direction, and geometric shape. We define an AR  
129 event as a series of spatiotemporally connected AR objects. The life cycle of an AR event  
130 represents the evolution of multiple overlapping AR objects within an AR event. The AR origin  
131 and termination are defined as the first and last AR objects in an AR life cycle, respectively. To  
132 identify an AR event and its life cycle, a tracking algorithm was developed in Zhou et al. (2018)  
133 that utilizes the spatial overlapping ratio between AR objects of consecutive time steps. An  
134 example of an identified landfalling AR event by Zhou et al (2018) is shown in Figure 1. This  
135 landfalling AR event originated over the central North Pacific and terminated over the Northwest  
136 U.S. during January 2018. The black dots are the centroids of AR objects, which are calculated  
137 as the mass-weighted mean latitudes and longitudes of the objects. The letters mark the centroids  
138 of origin (O) and termination (T) objects. This landfalling AR event lasted for 4.75 days (19 6-  
139 hourly time intervals).





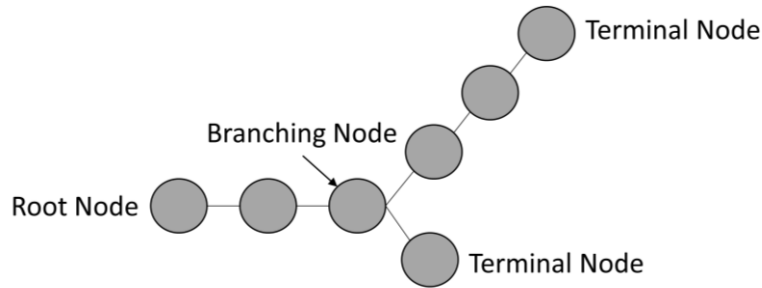
140

141 **Figure 1.** Example of a landfalling AR event (O→T) in January 2018. Each shading color  
 142 represents an instantaneous AR object from sequential time steps. The black dot marks the  
 143 centroid of each AR object. The red dots marked with “O” and “T” are the centroids of the origin  
 144 and termination objects, respectively. The red line connects the dots and represents the  
 145 propagation track of the landfalling AR event.

146

147 When AR objects propagate, it is possible that objects from different AR events merge  
 148 together or one object splits into multiple objects that propagate in different directions. In Zhou  
 149 et al (2018), the merging and splitting objects are marked as origins of new AR life cycles. While  
 150 marking merging and splitting objects as new origins may help to explain the merging or  
 151 splitting process, the AR events identified in this way may not represent the complete life cycle  
 152 of moisture transport. To capture the complete life cycles of landfalling AR events, we updated  
 153 the tracking algorithm from Zhou et al. (2018) so that the merging or splitting objects are  
 154 identified as intermediate objects rather than new origin objects in AR life cycles. The updated  
 155 tracking algorithm is based on the tree data structure (Sleator & Tarjan, 1983), which is a widely-  
 156 used data structure in computer science. The tree data structure contains a set of linked nodes  
 157 that are distributed hierarchically (Figure 2). Like the shape of a tree, this data structure starts

158 from a root node and moves forward to any linked internal nodes in the next hierarchy. Moving  
 159 forward, the tree structure may branch out, which means a single internal node is linked to  
 160 multiple nodes in the next hierarchy. Finally, each branch of the tree structure ends with a  
 161 terminal node. The life cycle of an AR event is similar to a tree structure. The origin (termination)  
 162 object is analogous to the root (terminal) node. The merging/splitting object is equivalent to the  
 163 branching node of the structure. For AR events, the spatiotemporal connectivity (overlapping) is  
 164 a measure of linkage in the sense of a tree structure, and the number of time steps in the life  
 165 cycle of an AR event equals the number of hierarchies in a tree structure.



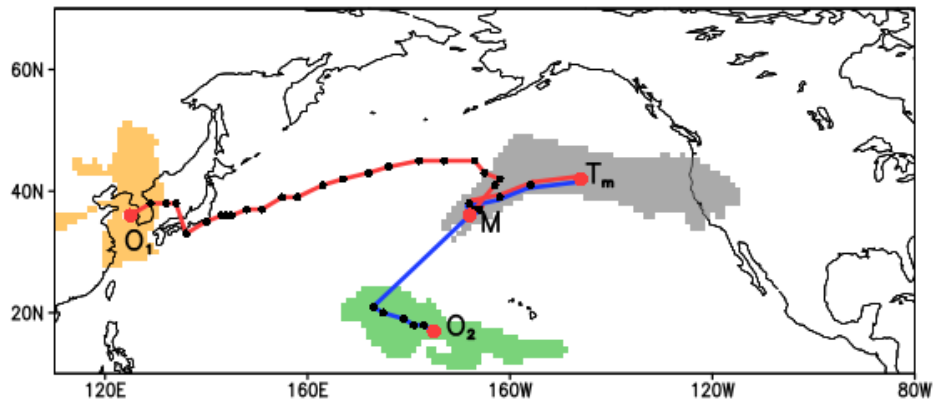
166

167 **Figure 2.** Schematic diagram of a tree structure. This tree structure starts at a root node, branches  
 168 off, and connects with two terminal nodes.

169

170 One of the classic algorithms used to traverse a tree structure is the depth-first search  
 171 (Tarjan, 1972). The depth-first search algorithm aims to find all the paths between the root node  
 172 (e.g., AR origin object) and the terminal node (e.g., AR termination object) and to track each  
 173 branch to the terminal node before moving to the next branch. The updated tracking algorithm  
 174 applies a depth-first search, which proceeds as follows: i) define the AR origin when an AR  
 175 object has no overlap with any object in the previous time step (Zhou et al. 2018); ii) starting  
 176 from the origins, repeatedly find the overlapping object in the next time step until termination  
 177 (no overlap with the next time step). If a splitting object occurs, each object after the splitting

178 will be tracked separately until termination so that one origin is connected to multiple  
 179 terminations. If multiple objects merge together, the life cycle after the merging object will be  
 180 linked to each of the objects before merging so that one termination can be linked to multiple  
 181 origins. Figure 3 shows an example of two merging AR events during December 2015 identified  
 182 by the updated tracking algorithm. One AR event originated on December 14 (orange shading,  
 183  $O_1$ ) and the other originated on December 18 (green shading,  $O_2$ ). The two events merged on  
 184 December 19 (point M) and terminated (grey shading,  $T_m$ ) on December 21. The correspondence  
 185 between one origin and one termination is recorded individually. For instance, the two AR events  
 186 in Figure 3 are recorded separately ( $O_1 \rightarrow T_m$  and  $O_2 \rightarrow T_m$ ), although they have the same  
 187 termination ( $T_m$ ). About 28% of total landfalling AR objects are recorded by more than one AR  
 188 event due to merging and splitting (such as  $M \rightarrow T_m$ ).



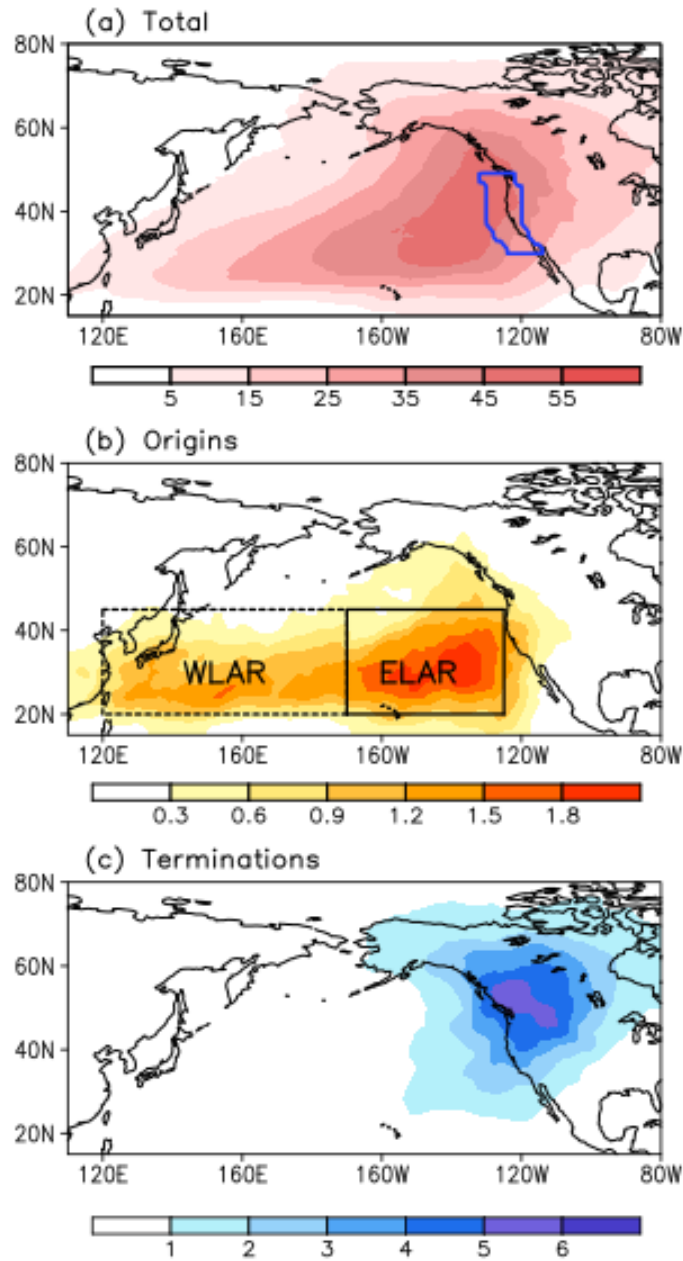
189  
 190 **Figure 3.** Example of merging AR events during December 2015. The two events originated  
 191 with different objects (orange ( $O_1$ ) and green ( $O_2$ ) shadings), merged, and terminated as the same  
 192 object (grey shading ( $T_m$ )). The red line ( $O_1 \rightarrow T_m$ ) and the blue line ( $O_2 \rightarrow T_m$ ) are the propagation  
 193 tracks of these two AR events, respectively. “M” marks the time step of merging.

194

### 195 3 Life-Cycle Characteristics by Distinct Origin Locations

196 We applied the updated algorithm to track landfalling AR events and record their life-  
197 cycle characteristics, including the locations of origin and termination, lifetimes, intensities, and  
198 propagation tracks. We identified a landfalling AR event as when an AR event has passed  
199 through a landfalling region over the U.S. West Coast (blue box in Figure 4a) during its life  
200 cycle. The landfalling region is selected along the U.S. West Coast (30°N-49°N) with a zonal  
201 width of ten 1° grid points. We tested the sensitivity of landfalling AR events to the landfalling  
202 region by zonally shifting the region by three grids or decreasing the zonal width by three grids.  
203 The identified landfalling AR events are not sensitive to the width of the landfalling region (not  
204 shown). Figure 4a shows the total AR frequency associated with landfalling AR events, which is  
205 the grid-point accumulated number of AR objects per winter. AR objects recorded in multiple  
206 AR events due to merging/splitting are counted only once in the calculation of AR frequency.  
207 The AR frequency spreads over the North Pacific with a maximum of over 45 objects per winter  
208 at each grid point between 30°N-60°N adjacent to the West Coast (Figure 4a). On average, about  
209 24 landfalling AR events per winter occur over the U.S. West Coast, which agrees with previous  
210 studies (Harris & Carvalho, 2018; Payne & Magnusdottir, 2014). With the tracking algorithm,  
211 we can identify the origin and termination objects (Figures 4b-c) from all detected objects  
212 associated with landfalling AR events shown in Figure 4a. The AR origin frequency mainly  
213 scatters between 20°N-45°N in the North Pacific, with the maximum frequency over the  
214 subtropical Northeast Pacific. A secondary peak in origin frequency locates over the Northwest  
215 Pacific near 160°E, which suggests that a large number of landfalling AR events originate from  
216 the Northwest Pacific, travel across the North Pacific basin, and make landfall over the U.S.  
217 West Coast. The high termination frequency over land is due to the massive moisture loss

218 through precipitation when ARs make landfall (Dettinger, 2013; Neiman et al., 2013; Ralph &  
 219 Dettinger, 2012).



220

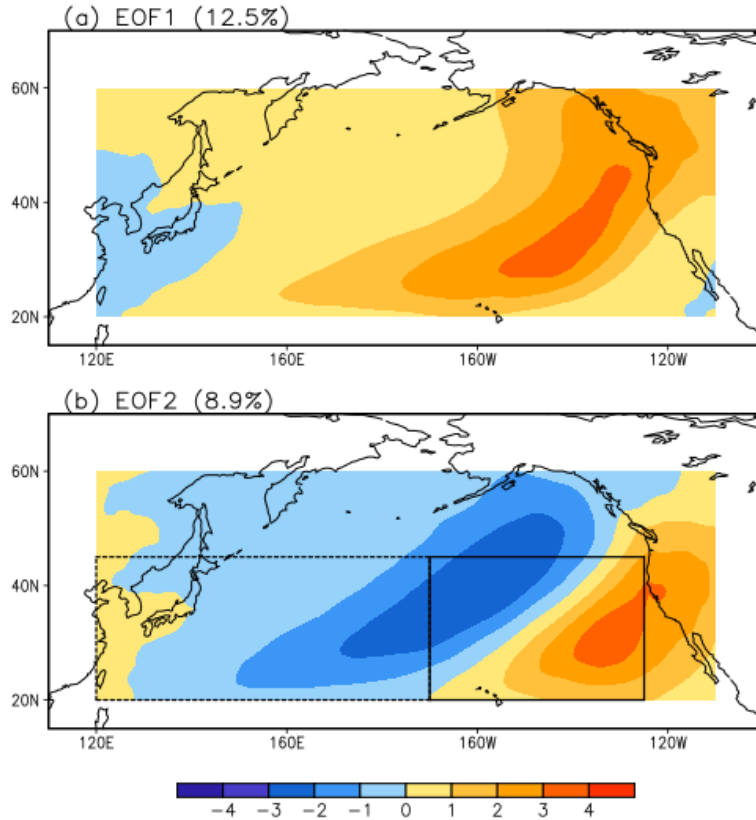
221 **Figure 4.** AR frequency (shading, number of objects per winter) for (a) total, (b) origin, and (c)  
 222 termination objects in landfalling AR events. The area enclosed by the blue line in (a) is the  
 223 region for landfalling AR event selection (10 longitudinal degrees along the U.S. West Coast  
 224 between 30°N-49°N). Boxes in (b) denote the origin locations of landfalling AR events from the

225 Northwest Pacific ( $20^{\circ}\text{N}$ - $45^{\circ}\text{N}$ ,  $120^{\circ}\text{E}$ - $170^{\circ}\text{W}$ ) (WLAR, dashed box) and landfalling AR events  
226 from the Northeast Pacific ( $20^{\circ}\text{N}$ - $45^{\circ}\text{N}$ ,  $125^{\circ}\text{W}$ - $170^{\circ}\text{W}$ ) (ELAR, solid box).

227

228 To compare the characteristics of landfalling AR events from different origin locations,  
229 we categorized the landfalling AR events into two groups based on their origin locations:  
230 landfalling AR events from the Northwest Pacific (WLAR events, dashed box in Figure 4b) and  
231 the Northeast Pacific (ELAR events, solid box in Figure 4b). To determine the domain for event  
232 selection, empirical orthogonal function (EOF) is applied to daily anomalous AR frequency  
233 ( $20^{\circ}\text{N}$ - $60^{\circ}\text{N}$ ,  $120^{\circ}\text{E}$ - $250^{\circ}\text{E}$ ) that are associated with landfalling AR events. To calculate daily  
234 anomalous AR frequency, we first summed the objects associated with landfalling AR events by  
235 every four 6-hourly time steps, then subtracted the daily climatology. Figure 5 shows the first  
236 two EOF modes. The first mode (12.5% variance explained) is a basin-scale monopole pattern of  
237 daily AR frequency over the entire North Pacific, which reflects the occurrence location of  
238 landfalling AR objects (Figure 5a). The second mode (8.9% variance explained) shows a west-  
239 east dipole pattern with the maxima over the Northeast Pacific around  $30^{\circ}\text{N}$ ,  $135^{\circ}\text{W}$  and the  
240 minima over the central Pacific near  $40^{\circ}\text{N}$ ,  $160^{\circ}\text{W}$  (Figure 5b). The second EOF mode could  
241 explain the variability of landfalling AR events from the Northeast Pacific ( $125^{\circ}\text{W}$ - $170^{\circ}\text{W}$ ) and  
242 from the Northwest Pacific ( $120^{\circ}\text{E}$ - $170^{\circ}\text{W}$ ). Therefore, we selected the two domains of origin  
243 locations based on the distinct west-east variation of daily AR frequency of landfalling AR  
244 events (Figure 4b). For 39 cool seasons, a total of 438 WLAR events and 499 ELAR events are  
245 selected for detailed analysis of landfalling AR life cycles.

246



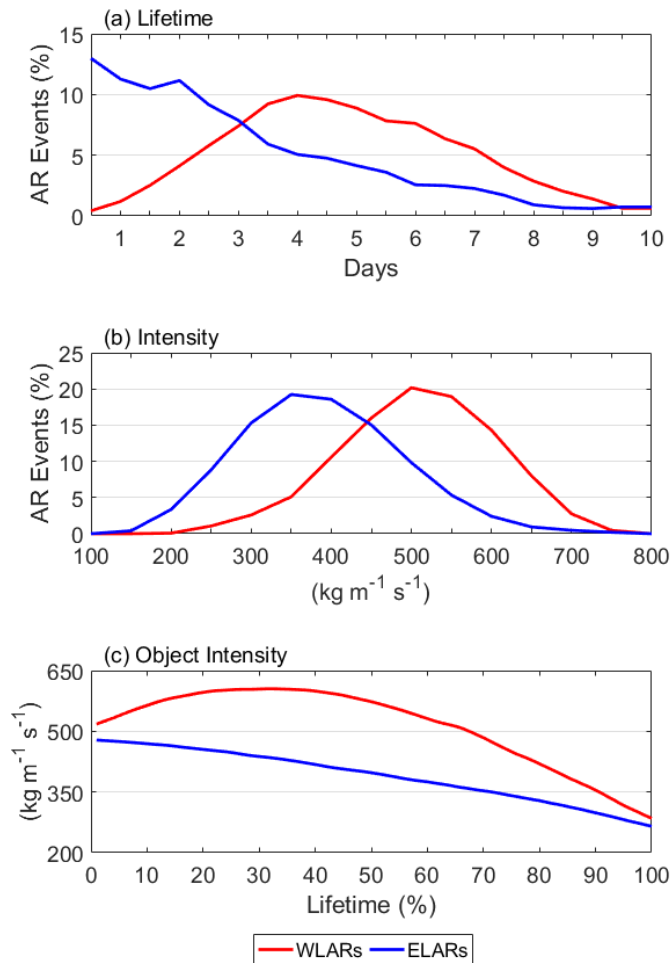
247

248 **Figure 5.** Spatial patterns of (a) the first and (b) second EOF modes of daily AR frequency  
 249 associated with landfalling AR events. The black boxes in (b) are the same as Figure 4(b) which  
 250 mark the selection domains for AR origins. The percentage shown in each panel's title represents  
 251 the variance explained by each mode.

252

253 The lifetime of an AR event is calculated as the product of the number of time intervals  
 254 between origin and termination, and the length of the time interval (6 hours). For example, the  
 255 lifetime of the landfalling AR event shown in Figure 1 is 4.75 days. Figure 6a shows the  
 256 probability density function (PDF) of the lifetimes of WLAR and ELAR events. For ELAR  
 257 events, the percentage gradually decreases as a function of lifetime. About 77% of ELAR events'  
 258 lifetimes persist less than 4 days (Figure 6a). We examined the ELAR events in the high tail of  
 259 the distribution (lifetime > 5.5 days, ~85<sup>th</sup> percentile) and found that the prolonged lifetimes of

260 those ELAR events are due to slow-moving AR objects or merging with other AR events (not  
 261 shown). The mean lifetime of ELAR events is 3.6 days, which is different from that of WLAR  
 262 events (5.3 days) on a 99% confidence level based on a two-sample t-test. About 60% of WLAR  
 263 events have lifetimes longer than 4 days because it requires more time for WLAR events to  
 264 travel across the North Pacific basin and reach the West Coast. The shorter-lived WLAR events  
 265 ( $< 2.5$  days,  $\sim 15^{\text{th}}$  percentile) mostly have origins closer to the central Pacific (not shown) and  
 266 longer-lived WLAR events ( $> 7$  days,  $\sim 85^{\text{th}}$  percentile) originate further west.  
 267



268  
 269 **Figure 6.** PDF of (a) lifetime (days), (b) mean intensity ( $\text{kg m}^{-1} \text{s}^{-1}$ ), and (c) change of object  
 270 intensity through the lifetime (percentage of lifetime) for WLAR (red) and ELAR (blue) events.



271

272           The intensity of an AR event is calculated as the average of objects' intensities which are  
273 the area-weighted mean IVT magnitudes within the AR objects. Figure 6b shows the PDF of the  
274 intensities of WLAR and ELAR events. The mean intensity is  $508 \text{ kg m}^{-1} \text{ s}^{-1}$  for WLAR events  
275 and  $388 \text{ kg m}^{-1} \text{ s}^{-1}$  for ELAR events, which are significantly different on a 99% confidence level  
276 based on a two-sample t-test. A previous study also showed that AR events originating from the  
277 western Pacific generally have stronger intensities than those from the eastern Pacific (Payne &  
278 Magnusdottir, 2014). To further understand why WLAR events have stronger intensities than  
279 ELAR events, we investigated the intensity changes during landfalling AR life cycles. Because  
280 the lengths of lifetimes vary among landfalling AR events (Figure 6a), we interpolated the time  
281 series of object intensity into 100 portions for every landfalling AR event for easier comparison.  
282 0% represents the origin and 100% represents the termination. For example, in Figure 1, 40% of  
283 the lifetime represents the first 1.9 days of the total 4.75 days. Figure 6c shows the temporal  
284 change in the object intensity of WLAR and ELAR events. WLAR events on average have  
285 stronger object intensity than ELAR events throughout their life cycles. The mean object  
286 intensity continuously decreases in ELAR events, whereas it increases during the first 20% of the  
287 lifetime and then gradually decreases for WLAR events (Figure 6c).

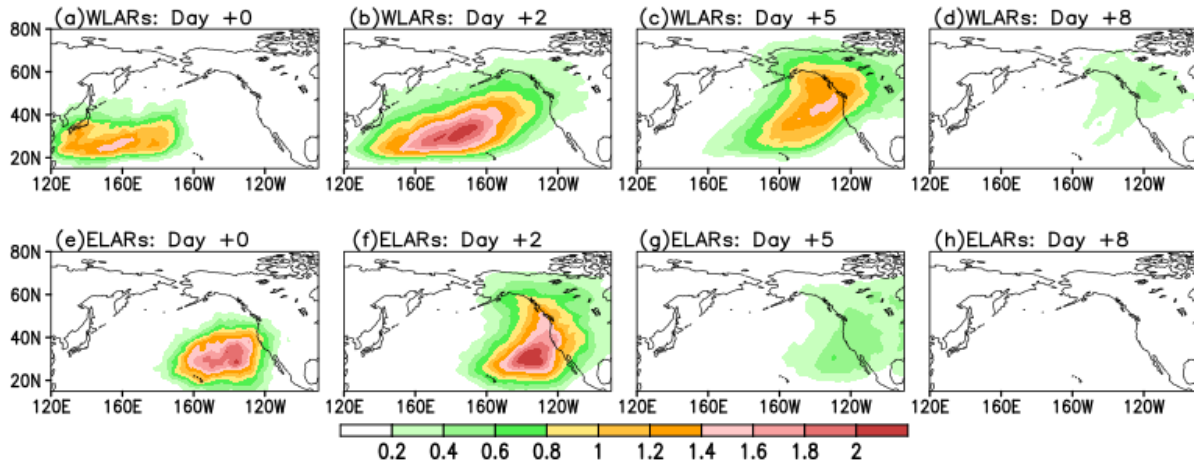
288

#### 289 **4 Distinct Evolutions of Landfalling AR Events**

290           To better understand the evolutions of landfalling AR events, we calculated the daily AR  
291 frequency starting from origins (Day +0) (Figure 7). Since the AR origins can occur in any of the  
292 four 6-hourly time steps during Day +0, we included the origin objects from all four time steps  
293 for Day +0 in Figure 7. After Day +0, only the AR objects at 00z are used and referred to as

294 daily for simplicity. A three-day (i.e., three 00z) moving average is performed after Day +0. For  
 295 example, Day +2 represents the average from Days +1 to +3.

296



297

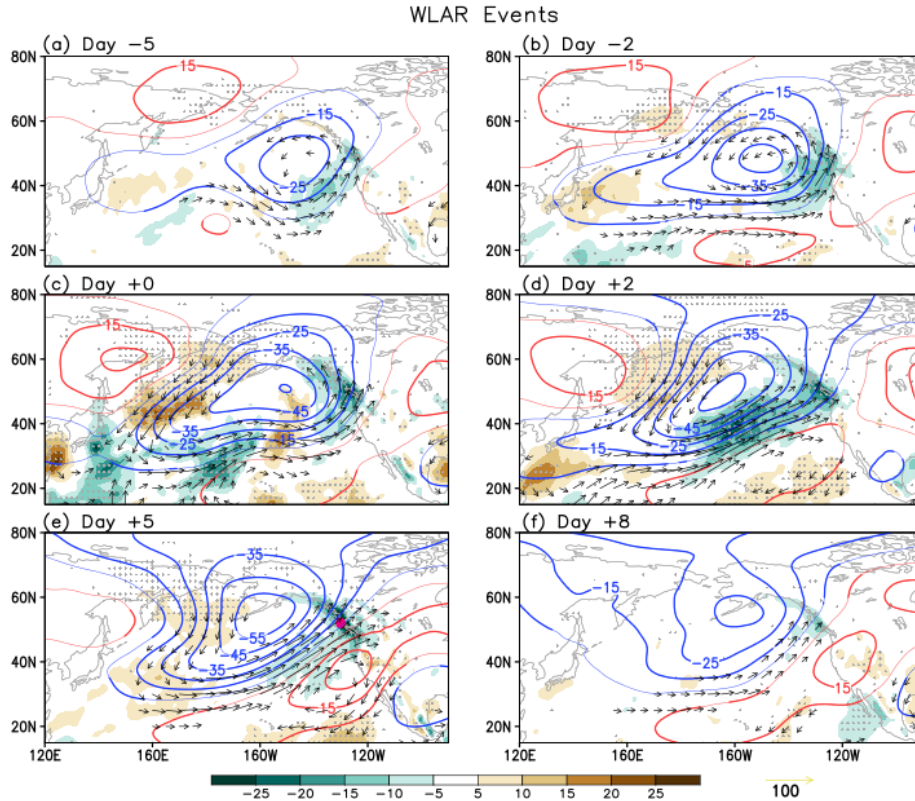
298 **Figure 7.** AR frequency (number of objects per winter) of (a-d) WLAR and (e-h) ELAR events  
 299 from Day +0 to Day +8. A three-day moving average is applied except for Day +0.

300

301 On Day +0, the origin objects of 438 WLAR events spread over the subtropical  
 302 Northwest Pacific with a maximum (over 1.4 objects per winter) between 20°N-30°N, 140°E-  
 303 170°E (Figure 7a). On Day +2, as objects of WLAR events propagate northeastward, the area  
 304 covered by WLAR objects enlarges over the North Pacific, with the maximum (over 2 objects  
 305 per winter) in the subtropical central Pacific (Figure 7b). The broad area of WLAR frequency  
 306 may be due to various propagation directions of WLAR events or intensification of WLAR  
 307 events as shown in Figure 6c. A few WLAR events make landfall over the West Coast on Day  
 308 +2 with less than 0.6 objects per winter over grid points in western North America (Figure 7b).  
 309 After Day +2, the overall WLAR frequency decreases due to the weakening of intensity (Figure  
 310 6c) or increasing number of terminated events. Day +5 is the peak landfall period for WLAR  
 311 events with over 0.8 object per winter between 40°N-70°N and roughly 1.4 objects per winter

312 near 50°N (Figure 7c). About 15% of all WLAR events last longer than 7 days and make landfall  
313 on Day +8 (Figure 6a and 7d). The landfalling latitudes of WLAR events are generally in the  
314 northwestern U.S. West Coast and British Columbia. Because ELAR events originate  
315 geographically closer to the U.S. West Coast, some ELAR events already extend to the West  
316 Coast on Day +0 with the maximum frequency of 1 object per winter over the grids near 35°N  
317 (Figure 7e). The ELAR frequency expands northward and reaches 70°N on Day +2 (Figure 7f).  
318 Day +2 is the peak landfall period for ELAR events. The ELAR frequency over the entire North  
319 American West Coast (25°N-60°N) is over 0.2 object per grid per winter, with a maximum of 1.6  
320 objects per winter near 35°N (Figure 7f). After the peak of landfall, the ELAR frequency  
321 decreases rapidly (Figures 7g-h).

322 To understand the evolution processes and large-scale patterns associated with the  
323 landfalling AR events, we calculated the composites of anomalous geopotential height at 500  
324 hPa (Z500), IVT, and moisture flux divergence from six days prior (Day -6) to nine days after  
325 (Day +9) landfalling AR origins (Figures 8 and 9). The selected time steps in Figures 8 and 9 are  
326 consistent with landfalling AR events shown in Figure 7. A three-day moving average is applied  
327 to the anomalous fields except for Day +0. For example, Day -5 represents the average of Day -  
328 6 to -4. For the significance test, a one-sample t-test is applied to the anomalous fields on each  
329 composite day. The significant values shown in Figure 8 and 9 represent that the value over the  
330 grid is 95% significantly different from the climatology for at least one day among the three-day  
331 averaging.



332

333 **Figure 8.** Daily composites of anomalous Z500 (contours, 10-meter interval, zero line is omitted,  
 334 red/blue contours represent positive/negative anomalies), IVT anomaly (vectors larger than 15 kg  
 335  $\text{m}^{-1} \text{s}^{-1}$ ), and anomalous moisture flux divergence (shading,  $1 \times 10^7 \text{ kg m}^{-1} \text{s}^{-1}$  interval) for WLAR  
 336 events. A three-day moving average is applied except for Day +0. The magenta dot in (e) marks  
 337 the location of maximum frequency during landfall. The dotted shading, thickened contours, and  
 338 vectors represent values that exceed the 95% confidence level of a one-sample t-test.

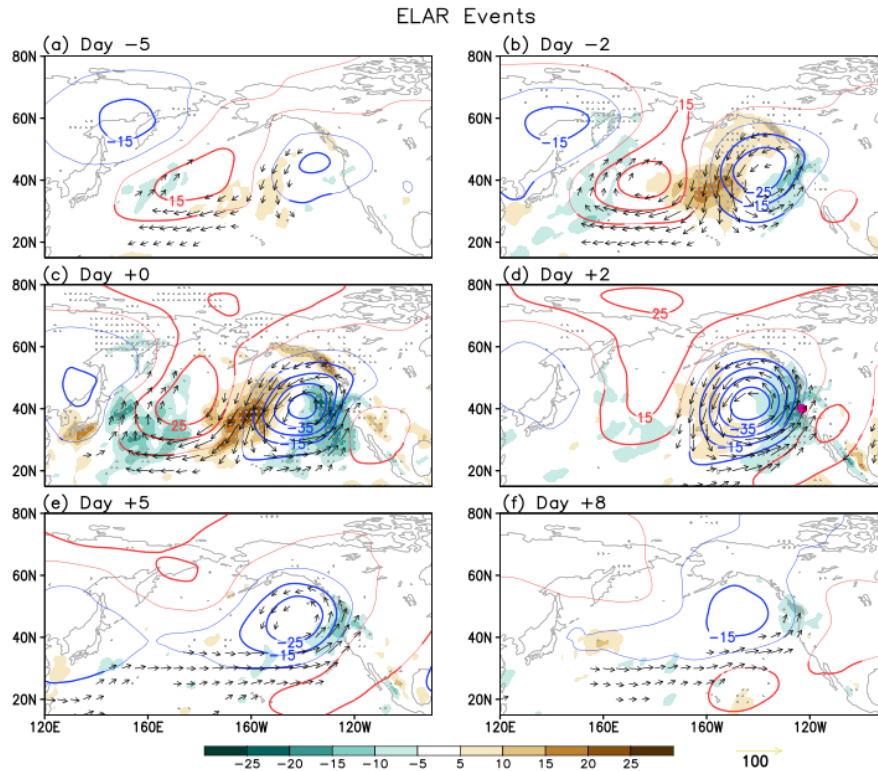
339

340 The life cycles of WLAR events are associated with a tripole pattern of geopotential  
 341 height anomalies over the North Pacific that persists for one week (from Day -2 to +5) with an  
 342 anomalous low over the central North Pacific and anomalous highs over northeast Asia and the  
 343 subtropical Northeast Pacific (Figure 8). A similar tripole pattern associated with landfalling  
 344 ARs over Oregon is shown in Benedict et al. (2019) by calculating lagged regression of

345 geopotential height onto the IVT at landfall. On Day  $-5$ , an anomalous high appears over  
346 northeastern Asia and an anomalous low emerges over the North Pacific (Figure 8a). As the two  
347 height anomalies intensify from Day  $-5$  to  $+0$ , the increasing pressure gradient induces an  
348 equatorward IVT anomaly and enhanced moisture flux divergence at the northwest side of the  
349 anomalous low (Figures 8a-c). The equatorward IVT decays from Days  $+2$  to  $+8$  with the  
350 weakening anomalous high over northeastern Asia (Figures 8d-f). Another anomalous high  
351 intensifies over the Northeast Pacific from Days  $-2$  to  $+5$ . Meanwhile, an eastward IVT anomaly  
352 and enhanced moisture flux convergence prevail between the anomalous low and high due to an  
353 increased pressure gradient (Figures 8b-e). The combination of the anomalous low and high  
354 modulates the origin and propagation of WLAR events. The eastward IVT anomaly supports the  
355 occurrence of WLAR origins on Day  $+0$ . Anomalous moisture flux convergence is induced over  
356 the Northwest U.S. and British Columbia during the landfall of WLAR events and persists until  
357 this tripole Z500 anomaly pattern dissipates on Day  $+5$  (Figures 8d-f).

358 A similar tripole pattern is shown associated with ELAR events but shifted eastward  
359 comparing to WLAR events (Figure 9). An anomalous high, which induces an anticyclonic  
360 circulation, persists over the northwestern Pacific from Days  $-5$  to  $+2$ . Correspondingly,  
361 equatorward (poleward) IVT and enhanced moisture flux divergence (convergence) remain at the  
362 east (west) side of the anomalous high from Days  $-5$  to  $+2$  (Figures 9a-d). On Day  $-2$ , an  
363 anomalous low, which modulates the occurrence and propagation of ELAR events, prevails over  
364 the Northeast Pacific (Figure 9b). As the anomalous low deepens, the IVT magnitude increases  
365 (not shown) and therefore leads to the origin of ELAR events (Figure 9c). On Day  $+0$ , another  
366 anomalous high appears over western Mexico. This anomalous high develops from Day  $+0$  to  $+2$   
367 and dissipates after Day  $+2$  (Figures 9c-f). The northward steering flow between the anomalous

368 low and high over the Northeast Pacific may be associated with the spread of landfalling  
 369 latitudes of ELAR events (Figure 9f). The maximum moisture flux convergence which is  
 370 associated with the landfalls of ELAR events appears further south compared to that of WLAR  
 371 events. The tripole anomalous Z500 pattern related to ELAR events persists for about one week  
 372 and gradually dissipates after Day +5 (Figures 9e-f) as ELAR events terminate (Figures 7g).



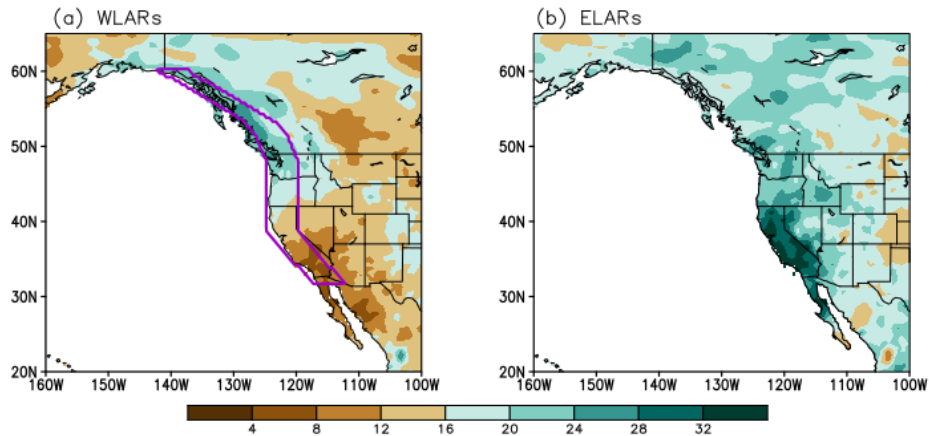
373  
 374 **Figure 9.** Same as Figure 8 but for ELAR events. The magenta dot in (d) marks the location of  
 375 maximum frequency during landfall.

376

### 377 5 AR-Induced Precipitation

378 To examine the precipitation related to WLAR and ELAR events, percentages of AR-  
 379 induced precipitation over the West Coast are calculated (Figure 10). We summed the daily  
 380 precipitation over 39 winters when an AR object made landfall and divided it by the total winter  
 381 precipitation accumulated over 39 winters. On average, about 40% of winter precipitation is

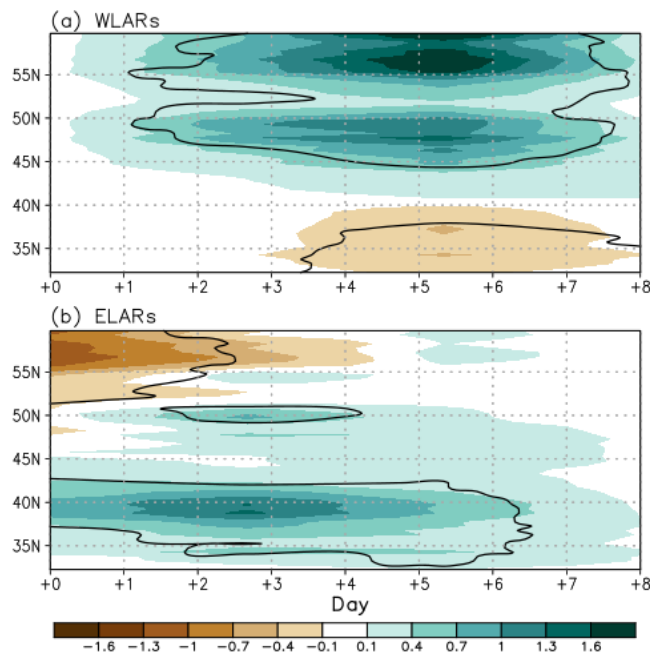
382 sourced from landfalling ARs over the West Coast, which is consistent with previous studies  
 383 (Dettinger et al., 2011; Gershunov et al., 2017; Guan et al., 2010, 2013; J. Kim et al., 2013). The  
 384 precipitation contributed by WLAR and ELAR events is compared in Figure 10. The percentage  
 385 of WLAR-induced precipitation increases from south to north, with about 10% in Southern  
 386 California, 10-20% in Northern California and Oregon, and 20-30% in British Columbia and  
 387 Washington (Figure 10a). The higher percentages (over 20%) between 45°N-60°N match well  
 388 with the area of enhanced moisture flux convergence and landfall latitudes (Figures 8d-e). The  
 389 percentage of precipitation induced by ELARs is about 30% over California, 20-30% over  
 390 Oregon and Washington, and 15-20% over British Columbia (Figure 10b). Overall, total winter  
 391 precipitation induced by ELAR events is higher than that by WLAR events, possibly due to the  
 392 ELAR events occurs more frequently in total (Figures 7).



393  
 394 **Figure 10.** Percentage (%) of AR-induced precipitation to total winter precipitation by (a)  
 395 WLAR and (b) ELAR events. The region with a width of five longitudinal degrees (10 grids in  
 396 0.5°) along the West Coast from 32°N-60°N (marked with the purple polygon in (a)) shows the  
 397 region for the zonal average shown in Figure 11.

398

399 To further understand the temporal changes of AR-induced precipitation, we calculated  
 400 the temporal evolution (starting from AR origins) of the AR-induced precipitation anomaly  
 401 (Figure 11, mm per event) zonally-averaged over the U.S. West Coast (enclosed purple polygon  
 402 in Figure 10a). The x-axis labels in Figure 11 are consistent with the subplot titles in Figures 7-9  
 403 where Day +0 represents the day of AR origin. A three-day moving average is also applied after  
 404 Day +0 in Figure 11. During the life cycle of every AR event, we include daily mean  
 405 precipitation only when an AR object is over land during the 10-day period. Since AR conditions  
 406 can persist for 24hr to 120hr after landfall (Payne & Magnusdottir, 2016; Ralph et al., 2013;  
 407 Ralph et al., 2011; Ralph et al., 2019), the precipitation caused by one landfalling AR event will  
 408 be counted in multiple consecutive days as long as the AR condition persists after landfall.



409 **Figure 11.** Evolution of AR-induced precipitation anomalies (shading, mm per event) averaged  
 410 along the West Coast (enclosed red polygon in Figure 10a) for (a) WLAR and (b) ELAR events.  
 411 Day +0 represents the AR origin. The areas enclosed by black contours are statistically  
 412



413 significant at the 95% confidence level based on a one-sample t-test. A three-day moving  
414 average is applied, except for Day +0.

415

416 For WLAR events, the increased AR-induced precipitation persists between 40°N-60°N  
417 from Days +2 to +8 with the maximum increase of over 2 mm per event between 55°N-60°N on  
418 Day +5 (Figure 11a). The increased precipitation on Day +2 corresponds with the enhanced  
419 moisture flux convergence induced by the anomalous low over the North Pacific (Figure 8d).  
420 The positive precipitation anomalies on Day +5 match with the peak of landfalling WLAR  
421 events (Figure 8e). Meanwhile, the reduced precipitation over the southern West Coast from  
422 Days +2 to +8 is associated with the enhanced moisture flux divergence between 20°N-40°N  
423 accompanied by the anomalous high over the Northeast Pacific (Figures 8d-f).

424 Positive precipitation anomalies appear between 35°N-45°N on Day +0 (Figure 11b)  
425 because some ELAR events reach the West Coast during their origins (Figure 7e). The positive  
426 precipitation anomalies last until Day +8 with a maximum increase of 1.3 mm per event between  
427 35°N-40°N on Days +2, which match with the peak landfall period of ELAR events (Figure 7f).  
428 The positive precipitation anomalies weaken after Day +2 due to the increasing number of  
429 terminated ELAR events (Figures 7g-h). The continuous positive precipitation anomalies from  
430 Days +5 to +8 may be due to persistent moisture support from the tropics or merging of events,  
431 which prolongs the lifetimes of ELAR events (long tail in Figure 6a). Meanwhile, negative  
432 precipitation anomalies appear between 50°N-60°N from Days +0 to +2, which is related to the  
433 moisture flux divergence anomaly associated with the anomalous high over the central North  
434 Pacific (Figures 9c-d).

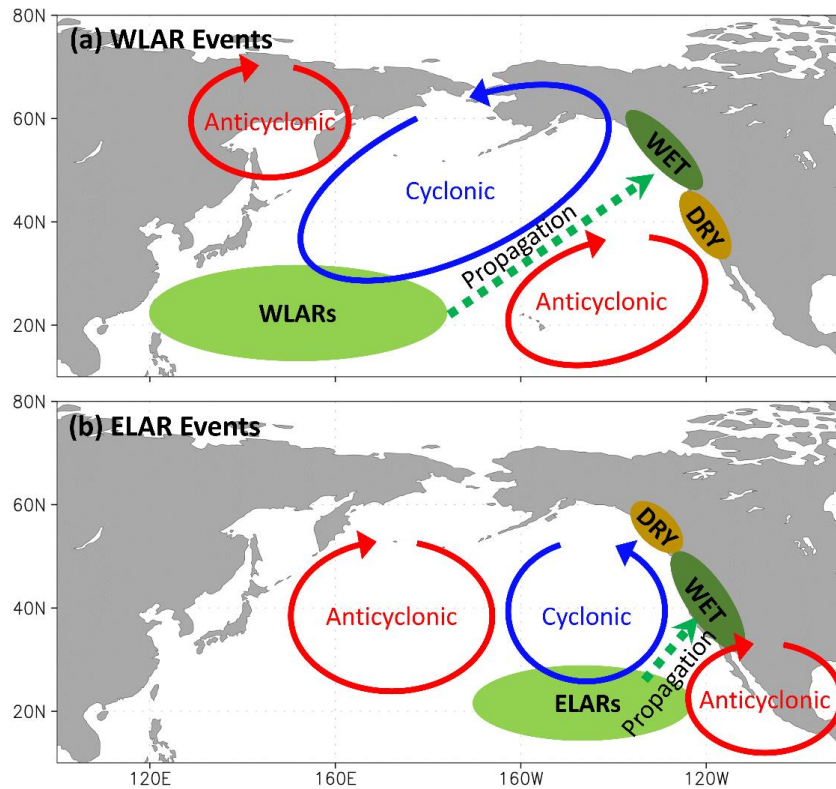
435

## 436 **6 Summary and Discussion**

437           To understand the impacts of distinct origin locations on the life cycles of AR events that  
438 make landfall over the U.S. West Coast, we investigated the landfalling AR events originating  
439 from the Northwest and Northeast Pacific by examining their life-cycle characteristics,  
440 associated circulation patterns, and precipitation anomalies during 39 winters from 1979 to 2018.  
441 We applied an AR tracking algorithm using a depth-first search to identify the life cycles of  
442 landfalling AR events. Generally, WLAR events are prone to landfall in the Northwest U.S. and  
443 British Columbia, while ELAR events have a vast range of landfalling latitudes along the U.S.  
444 West Coast. WLAR events have longer lifetimes and stronger intensities than ELAR events.

445           Two schematic diagrams are shown in Figure 12 to describe the distinct life cycles of  
446 WLAR and ELAR events. WLAR events are induced by northeastward IVT anomalies at the  
447 southeast side of the cyclonic circulation associated with an anomalous low over the central  
448 North Pacific (Figure 12a). Within 4-5 days after WLAR origins, maximum precipitation appears  
449 over the northern West Coast associated with the landfalls of WLAR events. The accumulated  
450 precipitation induced by WLAR events contributes 20-25% of the total winter precipitation over  
451 British Columbia and Washington. On the other hand, reduced precipitation occurs over the  
452 southern West Coast due to reduced moisture flux convergence associated with the anticyclonic  
453 flow anomaly over the Northeast Pacific. Such tripole pattern that shifts eastward is linked to the  
454 occurrence and propagation of ELAR events (Figure 12b). The anomalous low over the  
455 Northeast Pacific accelerates the cyclonic circulation, which enhances the northeastward IVT,  
456 triggers ELAR events, and supports their northeastward propagation. The ELAR events lead to  
457 maximum precipitation over the southern West Coast approximately 2 days after their origins.  
458 ELAR-induced precipitation produces up to 30% of total winter precipitation over California.

459 Meanwhile, reduced precipitation over the northern West Coast is attributed to the moisture flux  
 460 divergence anomaly. While previous work has shown the large-scale patterns associated with  
 461 precipitation over the west coast of North America (Benedict et al., 2019; Carrera et al., 2004;  
 462 Higgins et al., 2000; Jiang & Deng, 2011; Lackmann & Gyakum, 1999), our study further  
 463 demonstrates that the life cycle of AR events can serve as an indicator to show how the large-  
 464 scale patterns modulate the pathway of moisture transport prior to the precipitation over land.



465  
 466 **Figure 12.** Schematic diagrams for the large-scale patterns, evolutions, and precipitation  
 467 anomalies related to the life cycles of (a) WLAR and (b) ELAR events. Green ovals mark the  
 468 distinct origin locations. Dashed green arrows indicate the propagation direction of AR events.  
 469 Circle arrows denote the circulation direction where the blue (red) arrow indicates cyclonic  
 470 (anticyclonic) circulation. Green and brown colors represent wet and dry precipitation anomalies,  
 471 respectively.

472

473           Our results indicate that the life cycles of AR events can be useful tools to improve the  
474 forecasts of ARs and associated precipitation over the West Coast. With the empirical  
475 relationships discussed in this study, it may be possible to forecast the propagation track,  
476 termination location, and precipitation amount associated with a specific AR by knowing its  
477 origin location. In addition, since the signal of the tripole Z500 anomaly pattern occurs  
478 approximately 5 days prior to AR origins and persists for a week, the circulation patterns can be  
479 considered as potential precursors for landfalling AR events and therefore may help improve the  
480 subseasonal prediction of landfalling AR activity.

481           Recently, research interest has been growing in the subseasonal prediction of ARs  
482 because the subseasonal forecast is particularly important in making management decisions  
483 regarding water, agriculture, and hazards. Skillful prediction of weekly AR occurrence is  
484 maintained for up to 3 weeks (DeFlorio et al., 2018b) and can be further extended to 5 weeks by  
485 taking the MJO and Quasi-Biennial Oscillation into account (Baggett et al., 2017; Mundhenk et  
486 al., 2018). The MJO is a major source of subseasonal predictability for ARs because the MJO-  
487 induced tropical heating can modulate ARs by perturbing midlatitude geopotential heights via  
488 Rossby wave teleconnections (Guan et al., 2012; Payne & Magnusdottir, 2014; Ralph et al., 2011;  
489 Stan et al., 2017). Therefore, to further improve subseasonal AR prediction, it is crucial to  
490 understand the physical processes governing the MJO's modulation of ARs. The AR life cycle  
491 approach may help to extend the understanding of how the MJO influences AR activity by  
492 linking the spatiotemporal evolution of AR events to the propagation of the MJO. For example,  
493 by comparing the life cycles of AR events during different MJO phases, it is feasible to study the  
494 dynamical mechanisms of how the MJO's intensity, propagation, and teleconnection patterns

495 modulate the origin locations and evolutions of AR events, which has implications for a better  
496 understanding of AR activity and improving the subseasonal AR prediction.

497 **Acknowledgment**

498 Constructive and valuable comments from three anonymous reviewers are greatly appreciated.

499 YZ was supported by NSF grant AGS-1652289 and by the U.S. Department of Energy, Office of

500 Science, Office of Biological and Environmental Research, Climate and Environmental Sciences

501 Division, Regional & Global Climate Modeling Program, under Award Number DE-AC02-

502 05CH11231. HK was supported by NSF grant AGS-1652289 and the KMA R&D Program grant

503 KMI2018-03110. The sources of data used in this study are:

504 <http://apps.ecmwf.int/datasets/data/interim-full-daily/levtype=pl/> for ERA-Interim reanalysis;

505 <https://www.esrl.noaa.gov/psd/data/gridded/data.cpc.globalprecip.html> for CPC Global Unified

506 Gauge-Based Analysis of Daily Precipitation.

507

508

509 **Reference**

- 510 Baggett, C. F., Barnes, E. A., Maloney, E. D., & Mundhenk, B. D. (2017). Advancing  
511 atmospheric river forecasts into subseasonal-to-seasonal time scales. *Geophysical*  
512 *Research Letters*, 44(14), 7528-7536. doi:10.1002/2017gl074434
- 513 Benedict, J. J., Clement, A. C., & Medeiros, B. (2019). Atmospheric blocking and other large-  
514 scale precursor patterns of landfalling atmospheric rivers in the North Pacific: A CESM2  
515 study. *Journal of Geophysical Research: Atmospheres*, 0(ja). doi:10.1029/2019jd030790
- 516 Carrera, M. L., Higgins, R. W., & Kousky, V. E. (2004). Downstream weather impacts  
517 associated with atmospheric blocking over the northeast Pacific. *Journal of Climate*,  
518 17(24), 4823-4839. doi:10.1175/Jcli-3237.1
- 519 Dee, D. P., Uppala, S. M., Simmons, A. J., Berrisford, P., Poli, P., Kobayashi, S., et al. (2011).  
520 The ERA-Interim reanalysis: configuration and performance of the data assimilation  
521 system. *Quarterly Journal of the Royal Meteorological Society*, 137(656), 553-597.  
522 doi:10.1002/qj.828
- 523 DeFlorio, M. J., Waliser, D. E., Guan, B., Lavers, D. A., Ralph, F. M., & Vitart, F. (2018a).  
524 Global Assessment of Atmospheric River Prediction Skill. *Journal of Hydrometeorology*,  
525 19(2), 409-426. doi:10.1175/Jhm-D-17-0135.1
- 526 DeFlorio, M. J., Waliser, D. E., Guan, B., Ralph, F. M., & Vitart, F. (2018b). Global evaluation  
527 of atmospheric river subseasonal prediction skill. *Climate Dynamics*.  
528 doi:10.1007/s00382-018-4309-x
- 529 Dettinger, M. D. (2011). Climate Change, Atmospheric Rivers, and Floods in California - A  
530 Multimodel Analysis of Storm Frequency and Magnitude Changes. *Journal of the*

- 531 *American Water Resources Association*, 47(3), 514-523. doi:10.1111/j.1752-  
532 1688.2011.00546.x
- 533 Dettinger, M. D. (2013). Atmospheric Rivers as Drought Busters on the US West Coast. *Journal*  
534 *of Hydrometeorology*, 14(6), 1721-1732. doi:10.1175/Jhm-D-13-02.1
- 535 Dettinger, M. D., Ralph, F. M., Das, T., Neiman, P. J., & Cayan, D. R. (2011). Atmospheric  
536 Rivers, Floods and the Water Resources of California. *Water*, 3(2), 445-478.  
537 doi:10.3390/w3020445
- 538 Dominguez, F., Dall'erba, S., Huang, S., Avelino, A., Mehran, A., Hu, H., et al. (2018). Tracking  
539 an atmospheric river in a warmer climate: from water vapor to economic impacts. *Earth*  
540 *Syst. Dynam.*, 9(1), 249-266. doi:10.5194/esd-9-249-2018
- 541 Espinoza, V., Waliser, D. E., Guan, B., Lavers, D. A., & Ralph, F. M. (2018). Global Analysis of  
542 Climate Change Projection Effects on Atmospheric Rivers. *Geophysical Research Letters*,  
543 45(9), 4299-4308. doi:10.1029/2017gl076968
- 544 Gershunov, A., Shulgina, T., Clemesha, R. E. S., Guirguis, K., Pierce, D. W., Dettinger, M. D.,  
545 et al. (2019). Precipitation regime change in Western North America: The role of  
546 Atmospheric Rivers. *Scientific Reports*, 9. doi:ARTN 994410.1038/s41598-019-46169-w
- 547 Gershunov, A., Shulgina, T., Ralph, F. M., Lavers, D. A., & Rutz, J. J. (2017). Assessing the  
548 climate-scale variability of atmospheric rivers affecting western North America.  
549 *Geophysical Research Letters*, 44(15), 7900-7908. doi:10.1002/2017gl074175
- 550 Gimeno, L., Nieto, R., Vazquez, M., & Lavers, D. A. (2014). Atmospheric rivers: a mini-review.  
551 *Frontiers in Earth Science*, 2(2). doi:10.3389/feart.2014.00002



- 552 Guan, B., Molotch, N. P., Waliser, D. E., Fetzer, E. J., & Neiman, P. J. (2010). Extreme snowfall  
553 events linked to atmospheric rivers and surface air temperature via satellite measurements.  
554 *Geophysical Research Letters*, *37*. doi:Artn L2040110.1029/2010gl044696
- 555 Guan, B., Molotch, N. P., Waliser, D. E., Fetzer, E. J., & Neiman, P. J. (2013). The 2010/2011  
556 snow season in California's Sierra Nevada: Role of atmospheric rivers and modes of  
557 large-scale variability. *Water Resources Research*, *49*(10), 6731-6743.  
558 doi:10.1002/wrcr.20537
- 559 Guan, B., & Waliser, D. E. (2015). Detection of atmospheric rivers: Evaluation and application  
560 of an algorithm for global studies. *Journal of Geophysical Research-Atmospheres*,  
561 *120*(24), 12514-12535. doi:10.1002/2015jd024257
- 562 Guan, B., Waliser, D. E., Molotch, N. P., Fetzer, E. J., & Neiman, P. J. (2012). Does the  
563 Madden–Julian Oscillation Influence Wintertime Atmospheric Rivers and Snowpack in  
564 the Sierra Nevada? *Monthly Weather Review*, *140*(2), 325-342. doi:10.1175/mwr-d-11-  
565 00087.1
- 566 Hagos, S. M., Leung, L. R., Yoon, J. H., Lu, J., & Gao, Y. (2016). A projection of changes in  
567 landfalling atmospheric river frequency and extreme precipitation over western North  
568 America from the Large Ensemble CESM simulations. *Geophysical Research Letters*,  
569 *43*(3), 1357-1363. doi:10.1002/2015gl067392
- 570 Harris, S. M., & Carvalho, L. M. V. (2018). Characteristics of southern California atmospheric  
571 rivers. *Theoretical and Applied Climatology*, *132*(3-4), 965-981. doi:10.1007/s00704-  
572 017-2138-1

- 573 Higgins, R. W., Schemm, J. K. E., Shi, W., & Leetmaa, A. (2000). Extreme precipitation events  
574 in the western United States related to tropical forcing. *Journal of Climate*, *13*(4), 793-  
575 820. doi:10.1175/1520-0442(2000)013<0793:Epeitw>2.0.Co;2
- 576 Jiang, T. Y., & Deng, Y. (2011). Downstream modulation of North Pacific atmospheric river  
577 activity by East Asian cold surges. *Geophysical Research Letters*, *38*(20), n/a-n/a.  
578 doi:Artn L2080710.1029/2011gl049462
- 579 Kim, H., Zhou, Y., & Alexander, M. A. (2017). Changes in atmospheric rivers and moisture  
580 transport over the Northeast Pacific and western North America in response to ENSO  
581 diversity. *Climate Dynamics*, 1-14. doi:10.1007/s00382-017-3598-9
- 582 Kim, J., Waliser, D. E., Neiman, P. J., Guan, B., Ryoo, J. M., & Wick, G. A. (2013). Effects of  
583 atmospheric river landfalls on the cold season precipitation in California. *Climate*  
584 *Dynamics*, *40*(1-2), 465-474. doi:10.1007/s00382-012-1322-3
- 585 Lackmann, G. M., & Gyakum, J. R. (1999). Heavy Cold-Season Precipitation in the  
586 Northwestern United States: Synoptic Climatology and an Analysis of the Flood of 17–18  
587 January 1986. *Weather and Forecasting*, *14*(5), 687-700. doi:10.1175/1520-  
588 0434(1999)014<0687:hcsplit>2.0.co;2
- 589 Lavers, D. A., Allan, R. P., Villarini, G., Lloyd-Hughes, B., Brayshaw, D. J., & Wade, A. J.  
590 (2013). Future changes in atmospheric rivers and their implications for winter flooding in  
591 Britain. *Environmental Research Letters*, *8*(3). doi:Artn 03401010.1088/1748-  
592 9326/8/3/034010
- 593 Lavers, D. A., & Villarini, G. (2015). The contribution of atmospheric rivers to precipitation in  
594 Europe and the United States. *Journal of Hydrology*, *522*, 382-390.  
595 doi:10.1016/j.jhydrol.2014.12.010

- 596 Mundhenk, B. D., Barnes, E. A., & Maloney, E. D. (2016a). All-Season Climatology and  
597 Variability of Atmospheric River Frequencies over the North Pacific. *Journal of Climate*,  
598 29(13), 4885-4903. doi:10.1175/Jcli-D-15-0655.1
- 599 Mundhenk, B. D., Barnes, E. A., Maloney, E. D., & Baggett, C. F. (2018). Skillful empirical  
600 subseasonal prediction of landfalling atmospheric river activity using the Madden–Julian  
601 oscillation and quasi-biennial oscillation. *npj Climate and Atmospheric Science*, 1(1),  
602 20177. doi:10.1038/s41612-017-0008-2
- 603 Mundhenk, B. D., Barnes, E. A., Maloney, E. D., & Nardi, K. M. (2016b). Modulation of  
604 atmospheric rivers near Alaska and the US West Coast by northeast Pacific height  
605 anomalies. *Journal of Geophysical Research-Atmospheres*, 121(21), 12751-12765.  
606 doi:10.1002/2016jd025350
- 607 Nardi, K. M., Barnes, E. A., & Ralph, F. M. (2018). Assessment of Numerical Weather  
608 Prediction Model Reforecasts of the Occurrence, Intensity, and Location of Atmospheric  
609 Rivers along the West Coast of North America. *Monthly Weather Review*, 146(10), 3343-  
610 3362. doi:10.1175/Mwr-D-18-0060.1
- 611 Neiman, P. J., Ralph, F. M., Moore, B. J., Hughes, M., Mahoney, K. M., Cordeira, J. M., &  
612 Dettinger, M. D. (2013). The Landfall and Inland Penetration of a Flood-Producing  
613 Atmospheric River in Arizona. Part I: Observed Synoptic-Scale, Orographic, and  
614 Hydrometeorological Characteristics. *Journal of Hydrometeorology*, 14(2), 460-484.  
615 doi:10.1175/Jhm-D-12-0101.1
- 616 Payne, A. E., & Magnusdottir, G. (2014). Dynamics of Landfalling Atmospheric Rivers over the  
617 North Pacific in 30 Years of MERRA Reanalysis. *Journal of Climate*, 27(18), 7133-7150.  
618 doi:10.1175/Jcli-D-14-00034.1

- 619 Payne, A. E., & Magnusdottir, G. (2015). An evaluation of atmospheric rivers over the North  
620 Pacific in CMIP5 and their response to warming under RCP 8.5. *Journal of Geophysical*  
621 *Research-Atmospheres*, 120(21), 11173-11190. doi:10.1002/2015jd023586
- 622 Payne, A. E., & Magnusdottir, G. (2016). Persistent landfalling atmospheric rivers over the west  
623 coast of North America. *Journal of Geophysical Research-Atmospheres*, 121(22), 13287-  
624 13300. doi:10.1002/2016jd025549
- 625 Ralph, F. M., Coleman, T., Neiman, P. J., Zamora, R. J., & Dettinger, M. D. (2013). Observed  
626 Impacts of Duration and Seasonality of Atmospheric-River Landfalls on Soil Moisture  
627 and Runoff in Coastal Northern California. *Journal of Hydrometeorology*, 14(2), 443-459.  
628 doi:10.1175/Jhm-D-12-076.1
- 629 Ralph, F. M., & Dettinger, M. D. (2012). Historical and National Perspectives on Extreme West  
630 Coast Precipitation Associated with Atmospheric Rivers during December 2010. *Bulletin*  
631 *of the American Meteorological Society*, 93(6), 783-790. doi:10.1175/Bams-D-11-  
632 00188.1
- 633 Ralph, F. M., Neiman, P. J., Kiladis, G. N., Weickmann, K., & Reynolds, D. W. (2011). A  
634 Multiscale Observational Case Study of a Pacific Atmospheric River Exhibiting Tropical-  
635 Extratropical Connections and a Mesoscale Frontal Wave. *Monthly Weather Review*,  
636 139(4), 1169-1189. doi:10.1175/2010mwr3596.1
- 637 Ralph, F. M., Neiman, P. J., Wick, G. A., Gutman, S. I., Dettinger, M. D., Cayan, D. R., & White,  
638 A. B. (2006). Flooding on California's Russian River: Role of atmospheric rivers.  
639 *Geophysical Research Letters*, 33(13). doi:Artn L1380110.1029/2006gl026689

- 640 Ralph, F. M., Rutz, J. J., Cordeira, J. M., Dettinger, M., Anderson, M., Reynolds, D., et al.  
641 (2019). A Scale to Characterize the Strength and Impacts of Atmospheric Rivers. *Bulletin*  
642 *of the American Meteorological Society*, 0(0), null. doi:10.1175/bams-d-18-0023.1
- 643 Rutz, J. J., Steenburgh, W. J., & Ralph, F. M. (2014). Climatological Characteristics of  
644 Atmospheric Rivers and Their Inland Penetration over the Western United States.  
645 *Monthly Weather Review*, 142(2), 905-921. doi:10.1175/Mwr-D-13-00168.1
- 646 Ryoo, J. M., Kaspi, Y., Waugh, D. W., Kiladis, G. N., Waliser, D. E., Fetzer, E. J., & Kim, J.  
647 (2013). Impact of Rossby Wave Breaking on U.S. West Coast Winter Precipitation  
648 during ENSO Events. *Journal of Climate*, 26(17), 6360-6382. doi:10.1175/Jcli-D-12-  
649 00297.1
- 650 Ryoo, J. M., Waliser, D. E., Waugh, D. W., Wong, S., Fetzer, E. J., & Fung, I. (2015).  
651 Classification of atmospheric river events on the US West Coast using a trajectory model.  
652 *Journal of Geophysical Research-Atmospheres*, 120(8), 3007-3028.  
653 doi:10.1002/2014jd022023
- 654 Sellars, S. L., Kawzenuk, B., Nguyen, P., Ralph, F. M., & Sorooshian, S. (2017). Genesis,  
655 Pathways, and Terminations of Intense Global Water Vapor Transport in Association  
656 with Large-Scale Climate Patterns. *Geophysical Research Letters*, 44(24), 12465-12475.  
657 doi:10.1002/2017gl075495
- 658 Shields, C. A., Rutz, J. J., Leung, L. Y., Ralph, F. M., Wehner, M., Kawzenuk, B., et al. (2018).  
659 Atmospheric River Tracking Method Intercomparison Project (ARTMIP): project goals  
660 and experimental design. *Geoscientific Model Development*, 11(6), 2455-2474.  
661 doi:10.5194/gmd-11-2455-2018

- 662 Sleator, D. D., & Tarjan, R. E. (1983). A Data Structure for Dynamic Trees. *Journal of*  
663 *Computer and System Sciences*, 26(3), 362-391. doi:10.1016/0022-0000(83)90006-5
- 664 Smith, B. L., Yuter, S. E., Neiman, P. J., & Kingsmill, D. E. (2010). Water Vapor Fluxes and  
665 Orographic Precipitation over Northern California Associated with a Landfalling  
666 Atmospheric River. *Monthly Weather Review*, 138(1), 74-100.  
667 doi:10.1175/2009mwr2939.1
- 668 Stan, C., Straus, D. M., Frederiksen, J. S., Lin, H., Maloney, E. D., & Schumacher, C. (2017).  
669 Review of Tropical-Extratropical Teleconnections on Intraseasonal Time Scales. *Reviews*  
670 *of Geophysics*, 55(4), 902-937. doi:10.1002/2016rg000538
- 671 Tarjan, R. (1972). Depth-First Search and Linear Graph Algorithms. *SIAM Journal on*  
672 *Computing*, 1(2), 146-160. doi:10.1137/0201010
- 673 Waliser, D. E., & Guan, B. (2017). Extreme winds and precipitation during landfall of  
674 atmospheric rivers. *Nature Geoscience*, 10(3), 179-U183. doi:10.1038/Ngeo2894
- 675 Warner, M. D., Mass, C. F., & Salathe, E. P. (2015). Changes in Winter Atmospheric Rivers  
676 along the North American West Coast in CMIP5 Climate Models. *Journal of*  
677 *Hydrometeorology*, 16(1), 118-128. doi:10.1175/Jhm-D-14-0080.1
- 678 Wick, G. A., Neiman, P. J., Ralph, F. M., & Hamill, T. M. (2013). Evaluation of Forecasts of the  
679 Water Vapor Signature of Atmospheric Rivers in Operational Numerical Weather  
680 Prediction Models. *Weather and Forecasting*, 28(6), 1337-1352. doi:10.1175/Waf-D-13-  
681 00025.1
- 682 Xie, P. P., Yatagai, A., Chen, M. Y., Hayasaka, T., Fukushima, Y., Liu, C. M., & Yang, S.  
683 (2007). A Gauge-based analysis of daily precipitation over East Asia. *Journal of*  
684 *Hydrometeorology*, 8(3), 607-626. doi:10.1175/Jhm583.1

- 685 Zhou, Y., Kim, H., & Guan, B. (2018). Life Cycle of Atmospheric Rivers: Identification and  
686 Climatological Characteristics. *Journal of Geophysical Research: Atmospheres*, 0(ja).  
687 doi:10.1029/2018JD029180
- 688 Zhou, Y., & Kim, H. M. (2017). Prediction of atmospheric rivers over the North Pacific and its  
689 connection to ENSO in the North American multi-model ensemble (NMME). *Climate*  
690 *Dynamics*. doi:10.1007/s00382-017-3973-6
- 691 Zhu, Y., & Newell, R. E. (1994). Atmospheric Rivers and Bombs. *Geophysical Research Letters*,  
692 21(18), 1999-2002. doi:10.1029/94gl01710
- 693 Zhu, Y., & Newell, R. E. (1998). A proposed algorithm for moisture fluxes from atmospheric  
694 rivers. *Monthly Weather Review*, 126(3), 725-735. doi:10.1175/1520-  
695 0493(1998)126<0725:Apafmf>2.0.Co;2
- 696